

Interlayer Transition in a vdW Heterostructure toward Ultrahigh Detectivity Shortwave Infrared Photodetectors

Tailei Qi, Youpin Gong,* Alei Li, Xiaoming Ma, Peipei Wang, Rui Huang, Chang Liu, Ridwan Sakidja, Judy Z. Wu, Rui Chen,* and Liyuan Zhang*

Van der Waals (vdW) heterostructures of 2D atomically thin layered materials (2DLMs) provide a unique platform for constructing optoelectronic devices by staking 2D atomic sheets with unprecedented functionality and performance. A particular advantage of these vdW heterostructures is the energy band engineering of 2DLMs to achieve interlayer excitons through type-II band alignment, enabling spectral range exceeding the cutoff wavelengths of the individual atomic sheets in the 2DLM. Herein, the high performance of GaTe/InSe vdW heterostructures device is reported. Unexpectedly, this GaTe/InSe vdWs p–n junction exhibits extraordinary detectivity in a new shortwave infrared (SWIR) spectrum, which is forbidden by the respective bandgap limits for the constituent GaTe (bandgap of ≈ 1.70 eV in both the bulk and monolayer) and InSe (bandgap of ≈ 1.20 – 1.80 eV depending on thickness reduction from bulk to monolayer). Specifically, the uncooled SWIR detectivity is up to $\approx 10^{14}$ Jones at 1064 nm and $\approx 10^{12}$ Jones at 1550 nm, respectively. This result indicates that the 2DLM vdW heterostructures with type-II band alignment produce an interlayer exciton transition, and this advantage can offer a viable strategy for devising high-performance optoelectronics in SWIR or even longer wavelengths beyond the individual limitations of the bandgaps and heteroepitaxy of the constituent atomic layers.

to the bandgaps of 1.24–0.41 eV) are important for diverse applications in remote sensing, imaging, and free-space communications.^[1–4]

Conventional SWIR photodetectors rely on HgCdTe or InAs/GaSb type-II superlattices and InGaAs/GaAsSb type-II quantum wells, which encounter some fundamental obstacles.^[1,5–7] For example, the conventional HgCdTe with bandgaps tunable by the ternary chemical compositions suffers from raw material toxicity, poor material uniformity, and low yield. In addition, the HgCdTe SWIR photodetectors, similar to other SWIR photodetectors based on conventional narrowband semiconductors, must operate at cryogenic temperatures to suppress the dark current or thermal noise to ensure high detectivity. Furthermore, the conventional SWIR photodetectors based on type-II superlattices or multiple quantum wells require heteroepitaxy of constituent semiconductors using expensive molecular beam epitaxy systems.

Besides the high capital cost often limiting their applications primarily to military and high-end niche market, the stringent lattice match requirement in heteroepitaxy has been a fundamental bottleneck in the selection of suitable materials because


1. Introduction

Shortwave infrared (SWIR) photodetectors detecting lights in the wavelength spectrum of 1.0–3.0 μm (corresponding

T. L. Qi, Prof. Y. P. Gong, A. L. Li, Dr. X. M. Ma, Dr. P. P. Wang, R. Huang, Prof. C. Liu, Prof. L. Y. Zhang
Department of Physics
Southern University of Science and Technology
Shenzhen 518055, China
E-mail: gongyp@sustech.edu.cn; zhangly@sustech.edu.cn

Prof. Y. P. Gong
Academy for Advanced Interdisciplinary Studies
Southern University of Science and Technology
Shenzhen 518055, China

Prof. Y. P. Gong, Prof. R. Chen
Department of Electrical and Electronic Engineering
Southern University of Science and Technology
Shenzhen 518055, China
E-mail: chenr@sustech.edu.cn

 The ORCID identification number(s) for the author(s) of this article can be found under <https://doi.org/10.1002/adfm.201905687>.

Dr. X. M. Ma
Beijing National Laboratory for Condensed Matter Physics,
and Institute of Physics
Chinese Academy of Sciences
Beijing 100190, China

Prof. C. Liu
Shenzhen Institute for Quantum Science and Engineering
Southern University of Science and Technology
Shenzhen 518055, China

Prof. R. Sakidja
Department of Physics, Astronomy and Materials Science
Missouri State University
Springfield, MO 65897, USA

Prof. J. Z. Wu
Department of Physics and Astronomy
University of Kansas
Lawrence, KS 66045, USA

DOI: 10.1002/adfm.201905687

the strains induced by lattice mismatch of different layers can cause defects and therefore degrade the detector's performance. It is therefore vital and urgent to explore new uncooled, high-performance SWIR photodetectors.

2D van der Waals (vdW) heterostructures based on the combination of different 2D atomically thin layered materials (2DLMs) produced by layer-by-layer vertical stacking have shown outstanding advantages over conventional semiconductor quantum wells and superlattices by^[8–13] 1) eliminating the strict requirement of lattice match in heteroepitaxy of the constituent layers for desired functionalities; and 2) enabling versatile vdW interfaces for new optoelectronics of desired interface electronic structures. Of particular interest is the vdW heterostructures with type-II band alignment via interface energy band engineering, which would allow generation of interlayer excitons, or bound electron–hole pairs localized in different 2DLMs. By designing the type-II band alignment in the vdW heterostructures into SWIR spectrum, low-energy SWIR interlayer excitons that would otherwise be prohibited by the band-edge cutoffs in the constituent 2D layers can be generated, enabling photoexcited carrier generation by light absorption across a wider spectral range or even into the SWIR or mid/far-infrared band beyond the bandgap limit of individual 2DLMs.^[14–22] However, studies using the intriguing feature of the interlayer transition for SWIR photodetectors and their associated detection performance have been rarely reported so far. In some exploratory studies, photoresponse extended to SWIR was indeed observed.^[23,24]

Motivated by this, we report a comprehensive investigation of photodetection performance on a novel GaTe/InSe vdW heterostructures with type-II band alignment in this work. GaTe and InSe belong to group III–VI semiconductors and are promising candidates as building blocks for optoelectronics due to their unique optical and electronic properties. For example, GaTe (monoclinic) exhibits significant photosensitivity with a direct bandgap around 1.70 eV in both the bulk and 2D monolayer. On the other hand, the InSe (rhombohedral) has a high carrier mobility of $10^3 \text{ cm}^2 \text{ V}^{-1} \text{ s}^{-1}$ at room temperature and exhibits a direct-to-indirect bandgap transition when its thickness reduces from bulk to monolayer, accompanied with the variation of the bandgap from 1.20 to 1.80 eV.^[13,25–28] The ideal band diagram of the GaTe/InSe interface indicates that the GaTe/InSe vdW heterostructures are type-II band alignment.^[27,29–31] We have performed the density functional theory (DFT) calculations on the electronic structure of the GaTe/InSe vdW heterostructures, which shows that the InSe addition onto the GaTe layers can lead to lowering the bandgap, facilitating the interlayer exciton transitions in the GaTe/InSe vdW heterostructures. Quantitatively, the interlayer transition energy of 0.55 eV lies in the SWIR spectral range of 1.0–1.55 μm beyond the cutoff wavelengths of the constituent GaTe (0.73 μm) and InSe (0.95 μm). Experimentally, we successfully fabricated the GaTe/InSe vdW heterostructures using a layer-by-layer dry transfer method and achieved SWIR photodetection with excellent performance of unprecedented detectivity D^* values up to 10^{14} and 10^{12} Jones (1 Jones = $1 \text{ cm Hz}^{1/2} \text{ W}^{-1}$) at 1064 and 1550 nm at room temperature, respectively.

2. Results and Discussions

To assess the electronic structure and predict possible interlayer exciton transitions of the hybrid configuration made of heterogeneous 2D structures of InSe and GaTe, we initially performed the DFT calculations (Figure 1; Figures S1–S4 in the Supporting Information for the results from the individual phases).^[32–35] We included the van der Waals/dispersion interactions obtained from the DFT code of VASP.^[36] The details of our calculation procedures can be found in “Experimental Section” as well as in our previous publications.^[37] The heterostructure of GaTe/InSe as a model structure was constructed by having a continuous monolayer of GaTe with a cluster of InSe monolayer positioned atop the GaTe layer as shown in Figure 1a. This is a simple model to represent the two

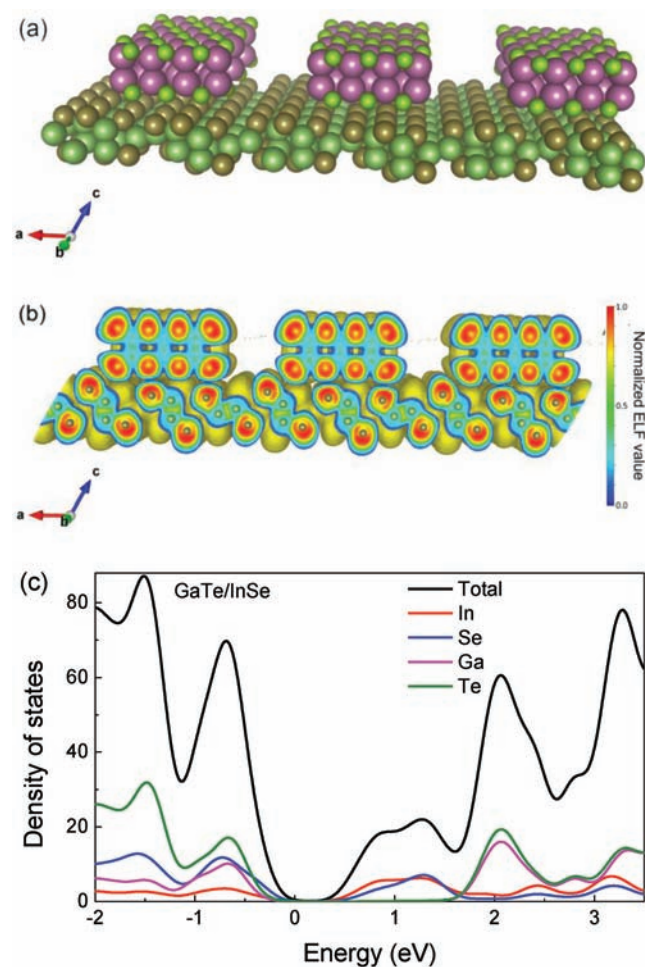


Figure 1. DFT calculation on the hybrid structure of InSe/GaTe. a) The atomic configuration of a simple model of the hybrid structure which is comprised of a continuous monolayer GaTe stacked by the monolayer of InSe dispersions. The purple and green spheres refer to In and Se atoms in InSe, respectively. The olive and dark yellow spheres refer to Ga and Te atoms in GaTe, respectively. b) The electron localization function (ELF) contour plots calculated using VASP to provide a better topological analysis of the chemical bonds between the 2D structures. c) Corresponding total and partial (based on atomic types) density of states.

heterogeneous 2D structures in stacking while allowing the InSe top monolayer to relax at the ground state. For the hybrid structure, we included sectioned electron localization function (ELF) plots orientated normal to a and b axes, respectively with 0.1 fractional increments along these axes. The ELF plots in general confirm the relatively low directional bonding between the two 2D structures as expected since the hybrid structure stability is provided by a weaker vdW bond. The bonding within each structure, however, is much stronger due to the presence of directional bonding facilitated by the hybridization between In and Se, and Ga and Te (Figure 1b). This is consistent with the results depicted in Figure 1c which shows the total and partial density of states (DOS) of the hybrid structure. The bandgap is now reduced from 1.3 eV to 0.5 eV for a monolayer of GaTe due to the contributions to partial DOS from In and Se into the original bandgap region of GaTe (Figure 1c). This new bandgap state is critical to enable the interlayer SWIR exciton generation and transition between the GaTe and InSe layers, illustrating the viability in bandgap engineering in the 2DLMs vdW heterostructures. In addition, to further confirm the thermal stability of the hybrid configuration, we performed ab initio molecular dynamics (AIMD) calculations on the hybrid GaTe/InSe structures under constant temperature and volume (NVT ensembles at 300 K) as also implemented in VASP code. The NVT is a standard term for the Molecular Dynamics ensembles (N = # of atoms, V = volume and T = temperature) that maintain a constant no. of atoms with a targeted constant average temperature controlled with a thermostat and under a constant volume of simulation box with a periodic boundary condition. The simulations showed the hybrid configurations remain relatively stable at 300 K as shown in the trajectory movie also provided in the Supporting Information.

The results of our DOS calculations suggested that the optical transition may be facilitated by means of the reduction

of the bandgap between valence and conduction bands for the hybrid structure. This is in reference to the originally wider bandgap of the GaTe 2D structure. The introduction of additional states at the conduction band donated by the 2D layer of InSe 2D allows for the additional optical transitions. The calculated bandgap obtained through DFT calculations has been known to underestimate that measured in the experimental results^[38] and our calculations are indeed no exception to this rule. The use of Heyd-Scuseria-Ernzerhof hybrid functionals^[39] helped increase the bandgap but overall the values remain lower than the experimental findings (bandgap of 2D GaTe = 1.7 eV), which is similar to that in other 2D materials.^[40] We should also note that due to the difference in the layer arrangement of stable phases of InSe and GaTe, there may be additional hybrid configurations that should be attainable, but an exhaustive exploration on these possibilities was beyond the scope of our current study, and it is expected to cause only negligible corrections to our current results. This may also affect the accuracy of the exact calculations on the bandgap. Nevertheless, the mechanism by which the optical transition is made possible through the additional inclusion of the conduction states to reduce the overall (now indirect) bandgap should remain valid.

Based on the theoretical predictions above, we fabricated the GaTe/InSe vdW heterostructure for SWIR photodetection using mechanical exfoliation of GaTe and InSe flakes from their corresponding bulk single crystals, followed with a layer-by-layer dry transfer to stack the flakes in the desired configuration (Figure 2). Figure 2a,b shows 3D schematic diagram and the optical image of a representative GaTe/InSe device, respectively. An atomic force microscopy (AFM) image (Figure S5, Supporting Information) illustrates the topography of the device and the extracted height profile which exhibits the thickness of the InSe and GaTe layers to be 8.1 nm (8 layers) and 7.3 nm (7 layers), respectively. Raman spectroscopy was employed to characterize

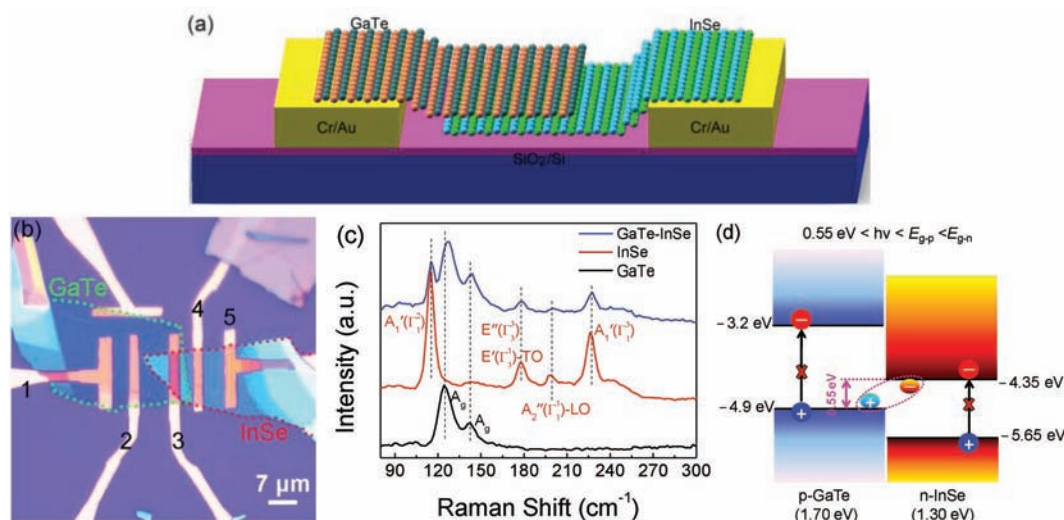


Figure 2. GaTe/InSe vdW heterostructure for SWIR photodetection. a) 3D schematic of the GaTe/InSe photodetector configuration. b) Optical image of a fabricated GaTe/InSe photodetector. Specifically, electrode pairs (E2/E4), (E1/E2), and (E4/E5) were used to measure the optoelectronic properties of the heterostructure, and individual GaTe and InSe devices, respectively. c) Raman spectra of the three regions of GaTe, InSe, and GaTe/InSe overlap in the device measured in the atmospheric condition under the 532 nm laser excitation. d) Schematic representation of the type-II band alignment of the GaTe/InSe vdW heterostructure and the corresponding principles of the interlayer transition at the interface. The $E_{g,p}$ and $E_{g,n}$ are the bandgap of p-GaTe and n-InSe, respectively.

the crystallinity of the individual GaTe and InSe flakes and the GaTe/InSe vdW heterojunction (where the two flakes overlap) (Figure 2c). The observed peaks at 126 and 144 cm^{-1} from individual GaTe (black line) correspond to the A_g modes of GaTe.^[41] For individual InSe (red line), the peaks at 115 cm^{-1} ($A'_1(\Gamma_1^2)$), 199 cm^{-1} ($A'_2(\Gamma_1^1)$ longitudinal optic phonon), 227 cm^{-1} ($A'_1(\Gamma_1^3)$) attribute to the out-of-plane phonon modes, while the peak at 179 cm^{-1} originates from the in-plane $E'(\Gamma_1^3)$ transverse optic phonon and $E''(\Gamma_1^3)$ phonons.^[42] Obviously, the Raman spectrum of the GaTe/InSe vdW junction (blue line) in the overlapped region comprises the Raman modes from the two constituent layers, which indicates the GaTe and InSe flakes in the junction region remain intact after the device fabrication. Figure 2d depicts schematically the band diagram of the GaTe/InSe vdW heterostructures device with a type-II band alignment based on electronic structures of the constituent GaTe and InSe layers and the GaTe/InSe interface.^[27,29–31] Interlayer exciton transitions are likely to occur and dominate the photoresponse when the photon energy is below the cutoffs of the p-GaTe (0.73 μm) and n-InSe (0.95 μm) and above the interlayer transition energy 0.5 eV. Specifically, this interlayer exciton transition photoresponse is located in the wavelength range of 1.0–1.55 μm .

In order to measure the photoresponse of interlayer exciton transition, two excitation lasers of 1550 and 1064 nm were employed to characterize the optoelectronic properties of the GaTe/InSe vdW heterostructures devices. Figure 3a,c shows the

current bias voltage ($I_{\text{ds}}-V_{\text{ds}}$) curves of the heterostructures in the dark (black line) and under different illumination powers at 1550 and 1064 nm lasers, respectively, which clearly demonstrates that the GaTe/InSe vdW heterostructure devices have an obvious photoresponse even under ultralow incident laser power (P_{in}) of 10^{-13} – 10^{-12} W. Considering the photoresponse in the wavelength range of 1.0–1.55 μm is beyond the cutoffs of the individual GaTe (0.73 μm) and InSe (0.95 μm) used for the GaTe/InSe vdW heterostructures, the observed SWIR photoresponse is a strong verification of the interlayer transition anticipated from the type-II band alignment at the GaTe/InSe vdW heterostructure interface. Quantitatively, the experimentally measured interlayer exciton energy cutoff around 0.55 eV (Figure 2d) agrees well with the DFT simulated one 0.5 eV. Moreover, anticipated nonlinear behavior of $I_{\text{ds}}-V_{\text{ds}}$ characteristics was observed, which is attributed to the p–n junction formed at the p-GaTe/n-InSe interface.^[43] The photocurrent, I_{ph} , can be extracted from the $I_{\text{ds}}-V_{\text{ds}}$ curves by subtracting the dark current (I_{dark}) from the current under illumination (I_{light}): $I_{\text{ph}} = I_{\text{light}} - I_{\text{dark}}$. Obviously, the I_{ph} of the devices exhibits a linear dependence on the V_{ds} (Figure 3b and the inset in Figure 3c), which indicates that larger I_{ph} values can be conveniently achieved by increasing the applied bias voltages across the source and drain electrodes of the GaTe/InSe devices. The dynamic photocurrent of the GaTe/InSe vdW heterostructure devices in response to the modulated incident light was measured at room temperature and the result is shown in Figure 3d and Figure S6 (Supporting

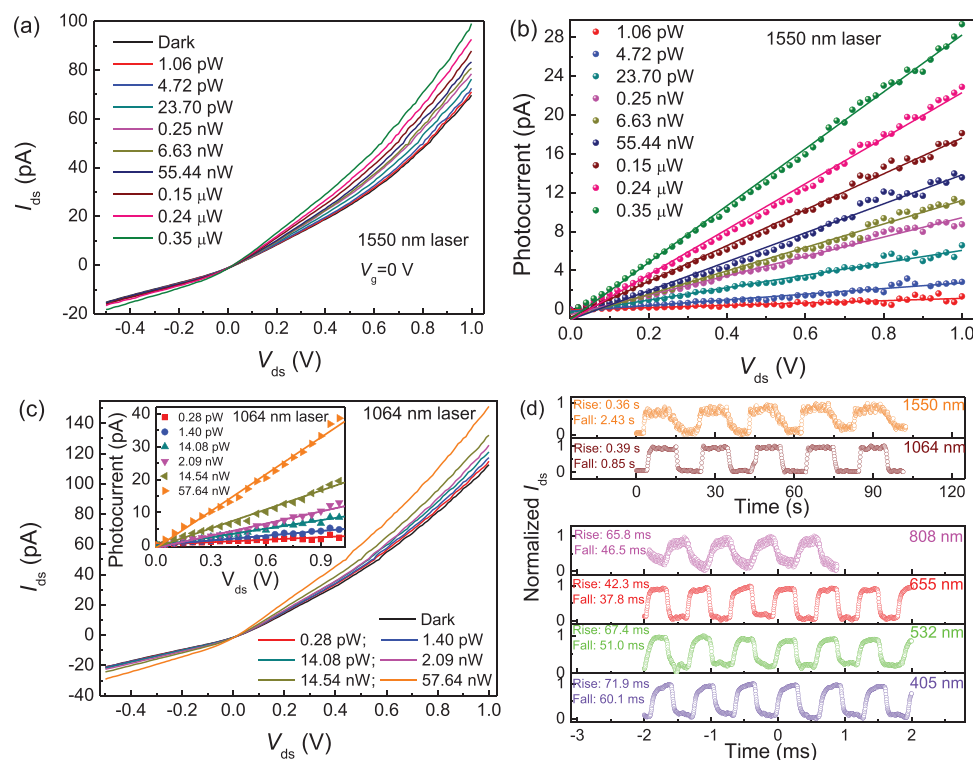


Figure 3. Optoelectronic characterization of the GaTe/InSe vdW heterostructure. a) $I_{\text{ds}}-V_{\text{ds}}$ curves in the dark and under 1550 nm laser with various powers measured at $V_g = 0$ V. b) $I_{\text{ph}}-V_{\text{ds}}$ curves at an excitation wavelength of 1550 nm with various powers, showing a linear dependence on the bias voltage. c) $I_{\text{ds}}-V_{\text{ds}}$ curves in the dark and under 1064 nm laser illumination with different powers. The inset shows a linear dependence of photocurrent on the bias voltage. d) Temporal photocurrent response under various excitation wavelengths. Measurements were carried out at room temperature in the atmosphere at $V_{\text{ds}} = 1$ V and $V_g = 0$ V.

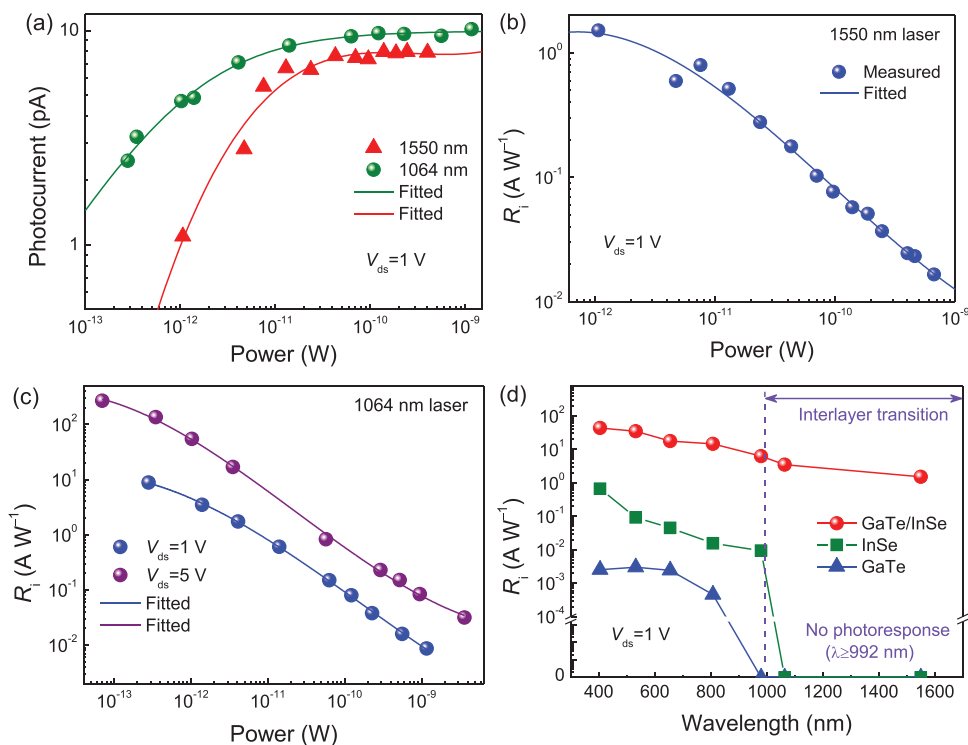


Figure 4. Photoresponse of the GaTe/InSe vdW heterostructure. a) Power dependence of photocurrent under 1064 and 1550 nm laser illuminations. b) Responsivity versus power under 1550 nm laser at $V_g = 0$ V and $V_{ds} = 1$ V. c) R_i as a function of power under 1064 nm laser at different bias values of 1 and 5 V at $V_g = 0$ V. d) Responsivity as a function of the wavelength obtained in the GaTe/InSe vdW heterostructure (red, with $P_{in} = 1.1$ – 2.2 pW) and individual InSe (olive) and GaTe (blue) devices.

Information). The rise/fall times can be estimated from the time spans when photocurrent increases/decreases between 10% and 90% of the stable maximum photocurrent at laser on/off. In the excitation wavelengths from the UV (405 nm) to NIR (980 nm) light, the response time of the device is in the range of 40–70 ms, while it increases by one order of magnitude under SWIR excitation (1064–1550 nm).

To give further insight into the performance of the GaTe/InSe vdW heterostructure photodetectors, the effects of laser power and bias voltage on photocurrent at various excitation wavelengths from visible light to SWIR are illustrated in Figure 4a and Figure S7 (Supporting Information). The I_{ph} first increases rapidly with increasing laser power at lower powers up to 20 pW and then almost reaches saturation as the incident light power reaches a higher level (Figure 4a). The responsivity R_i can be calculated using the equation $R_i = I_{ph}/P_{in}$. The I_{ph} increases with rising bias voltage and incident power (Figure S7, Supporting Information), indicating that the R_i of the devices would increase with increasing bias voltage and decreasing input optical power (Figure 4b,c; Figure S8, Supporting Information). Impressively, the R_i values of the GaTe/InSe vdW heterostructure photodetectors are 8.8 and 1.5 $A W^{-1}$ at $V_{ds} = 1$ V under a low incident light power of 10^{-12} – 10^{-13} W, corresponding to excitation wavelengths at 1064 and 1550 nm, respectively (Figure 4b,c). Because of the linear dependence of the photocurrent on the bias voltage (Figure 3b,c), the resulting R_i will increase to 267.4 $A W^{-1}$ under 1064 nm laser when applying a slightly larger V_{ds} to 5 V (Figure 4c). In addition, the GaTe/InSe vdW heterostructure SWIR photodetector also

shows broadband photoresponse in a wide spectrum range from 400 to 1550 nm (Figure S9, Supporting Information), which makes it potential hosts for multispectral detection. It should be pointed out that the R_i in the SWIR (at 1 V bias) with only interlayer excitation is about 100 times smaller than in the visible range in which the intralayer excitation dominates. This is consistent with previous experimental results^[44] and theoretical predictions^[45] that the oscillator strength of the interlayer excitons is smaller than that of the intralayer excitons by two orders of magnitude due to the spatial separation of electron–hole pairs confined to the opposite layers, resulting in a reduced photocurrent.

To shed lights on the response mechanism of GaTe/InSe vdW heterostructure SWIR photodetectors, we have fabricated control devices based on the individual GaTe and InSe flakes, respectively. The photoresponse performance of these devices is depicted in Figure S10 (Supporting Information). The R_i as a function of the wavelength in the GaTe/InSe heterostructure devices is compared with that in the individual GaTe and InSe devices, as detailed in Figure 4d. There are three fundamental differences between the GaTe/InSe vdW heterostructure photodetector and the individual GaTe and InSe devices. First, the GaTe/InSe vdW heterostructure photodetector exhibits considerably higher R_i over a wide wavelength range from the UV to NIR, typically by at least 2–4 orders of magnitude, as compared to the individual GaTe and InSe devices. This can be attributed to 1) the built-in electric field on the p-GaTe/n-InSe heterostructures, which can effectively facilitate the exciton dissociation for photocurrent and enhance R_i . In contrast, exciton dissociation

may be dramatically weak due to lack of a built-in field in the individual GaTe and InSe devices; and 2) the light absorption in the GaTe/InSe heterostructures composed of multiple photoactive layers is stronger than in the individual GaTe and InSe devices of only one type of flakes. The other difference is in dramatical reduction (or even unmeasurable photoresponse) on the individual GaTe and InSe devices when the wavelength is greater than 980 nm (808 nm) in the InSe (GaTe) device. This is not surprising considering the cutoff wavelengths of the 7–8 nm thick InSe and GaTe layers are 0.95 and 0.73 μm , respectively, which are consistent with previous theoretical calculations for DOS of the bulk and single layer (Figures S1–S4, Supporting Information). In addition, we found that the responsivity of GaTe/InSe decreases by less than a factor of 3 when exciting from 655 to 980 nm light, which is smaller than that of the individual GaTe and InSe cases (the R_i decreases at least by a factor of 10). This may be attributed to fact that the photoresponse of the GaTe/InSe heterostructures is the superposition of the photoresponses from its constituents of GaTe, InSe, and GaTe/InSe. The high responsivity at wavelength 980 nm in the GaTe/InSe heterostructures suggests that the contribution of the GaTe/InSe heterostructures is substantial even in the shorter-wavelength range. This explains the smaller decrease of the responsivity with increasing wavelengths in the GaTe/InSe vdW heterostructures. Therefore, the SWIR detection capability with a high R_i in the GaTe/InSe heterostructure device, beyond the bandgap limitation of individual GaTe and InSe, can be attributed to the occurrence of interlayer exciton generation and the subsequent separation of carriers driven by the built-in electric field at the p–n junction. Note that the laser power is varied in a wide range from 10^{-7} to 10^{-13} W during the measurement of the two types of devices, namely, heterostructures and single devices. It is found that the single GaTe or InSe photodetectors can only detect light with the power exceeding 10^{-11} W, as shown in Figure S10 in the Supporting Information. In contrast, the GaTe/InSe heterostructure photodetectors show a much higher sensitivity with a direct measurement of 10^{-13} W at 1064 nm (Figures 3c and 4c) and 10^{-12} W at 1550 nm (Figures 3a and 4b), which reflects the superiority of the GaTe/InSe heterostructure devices compared to the single GaTe or InSe device.

The spectra of current noise power density (I_n^2) in the dark were measured, and the noise equivalent power (NEP) was also calculated to determine the sensitivity of the photodetectors, as shown in Figure 5a,b. The I_n^2 spectra show two typical regions where a $1/f$ noise behavior dominates in the low-frequency region of $f < 1$ kHz and a generation–recombination (g–r) noise behavior occupies the region of $f > 1$ kHz, which resembles most p–n vdW heterojunction photodetectors. The NEP is equal to the signal power required for the ratio of the signal to noise to be unity with the unit of $\text{W Hz}^{-1/2}$, which is obtained by

$$\text{NEP} = \left(\overline{i_n^2}\right)^{1/2} / R_i = \text{RMS}(i_n) / R_i \quad (1)$$

where the $\text{RMS}(i_n) = \left(\overline{i_n^2}\right)^{1/2}$ is the root mean square (RMS) noise current, and the value of 1.29×10^{-15} A $\text{Hz}^{-1/2}$ can be calculated from the I_n^2 spectra in Figure 5a. The smallest NEP value obtained under 1550 nm illumination is 8.49×10^{-16} W $\text{Hz}^{-1/2}$

at $V_{ds} = 1$ V under an ultralow incident power of 1.1 pW. In addition, over the entire wavelength range from UV light (405 nm) to SWIR light (1550 nm), the NEP values lie in the range of 7.19×10^{-18} – 8.49×10^{-16} W $\text{Hz}^{-1/2}$ at $V_{ds} = 1$ V under low illumination power (Figure 5b; Figure S11, Supporting Information). This NEP is lower than the previously reported results in vdW heterostructures by at least two orders of magnitude,^[27,46,47] indicating that the GaTe/InSe heterostructure device has excellent sensitivity. This may be attributable to the suppression of random fluctuations of carriers by the potential barrier at the high-quality GaTe/InSe p–n junction.

The figure of merit—specific detectivity D^* was evaluated on the GaTe/InSe vdW heterostructure SWIR photodetectors. The D^* in the unit of $\text{cm Hz}^{1/2} \text{W}^{-1}$ is defined by $D^* = A^{1/2} / \text{NEP}$, where the A is the photosensitive area of the photodetector. The D^* values over the entire spectral range from UV to SWIR are shown in Figure 5c. The calculated D^* value is up to 10^{14} – 10^{13} Jones from the UV to the visible region and the D^* values are as high as 5.28×10^{12} and 9.12×10^{11} Jones at a bias of 1 V for the excitation wavelengths at 1064 and 1550 nm, respectively. Moreover, the D^* at 1064 nm illumination increases to 1.11×10^{14} Jones when the bias applied to the device was increased to 5 V (inset in Figure 5c). Impressively, the D^* of our GaTe/InSe devices is comparable to or even better than various state-of-the-art commercially available infrared detectors based on the InGaAs and InAs narrow-bandgap semiconductors, HgCdTe, InAs/GaSb type-II superlattices, and InGaAs/GaAsSb type-II multiple quantum wells (10^{11} – 10^{12} Jones at 1550 nm). Moreover, the D^* value of our GaTe/InSe devices is nearly 2–3 orders of magnitude higher than the best-reported value in 2D vdW heterostructures photodetectors^[48,49] such as black phosphorus/MoS₂ photodiode (2.13×10^9 Jones at 1550 nm) and MoS₂/graphene/WSe₂ photovoltaic detectors (10^{10} Jones at 1550 nm). A comparison of the performances is summarized in Table S1 (Supporting Information). More importantly, the D^* has no significant attenuation and remains at 10^{12} Jones as the excitation wavelength extends to the NIR or SWIR regime. Especially, by applying a slightly higher bias (5 V) to the device, we are able to achieve higher D^* (10^{13} – 10^{14} Jones) in the NIR range (inset in Figure 5c; Figure S12, Supporting Information), which illustrates that the GaTe/InSe vdW heterostructure device may be a superior candidate for uncooled SWIR detection.

The D^* of photodetectors is determined by the detection sensitivity, spectral response, and noise. To unveil the origin and the mechanism responsible for the high D^* of the GaTe/InSe vdW heterostructure device, we estimate the D^* values in another way by $D^* = R_i A^{1/2} / (2e I_{\text{dark}})^{1/2}$, where e is the elementary charge and I_{dark} is the dark current. The calculated D^* values are 1.55×10^{12} and 2.62×10^{11} Jones at a bias of 1 V for the excitation wavelengths at 1064 and 1550 nm, respectively, which is consistent with the value calculated (Figure 5c) by measuring the noise spectrum. This indicates that the dark current corresponding the shot noise and generation–recombination mainly contributes to the noise of our devices. The dark current densities (J) of our GaTe/InSe devices is 0.09–0.11 mA cm^{-2} at 1 V bias at room temperature (Figure S13, Supporting Information), which is reduced by almost two orders of magnitude compared to these conventional devices of InAs/GaSb type-II superlattices and InGaAs/GaAsSb type-II quantum wells (typically

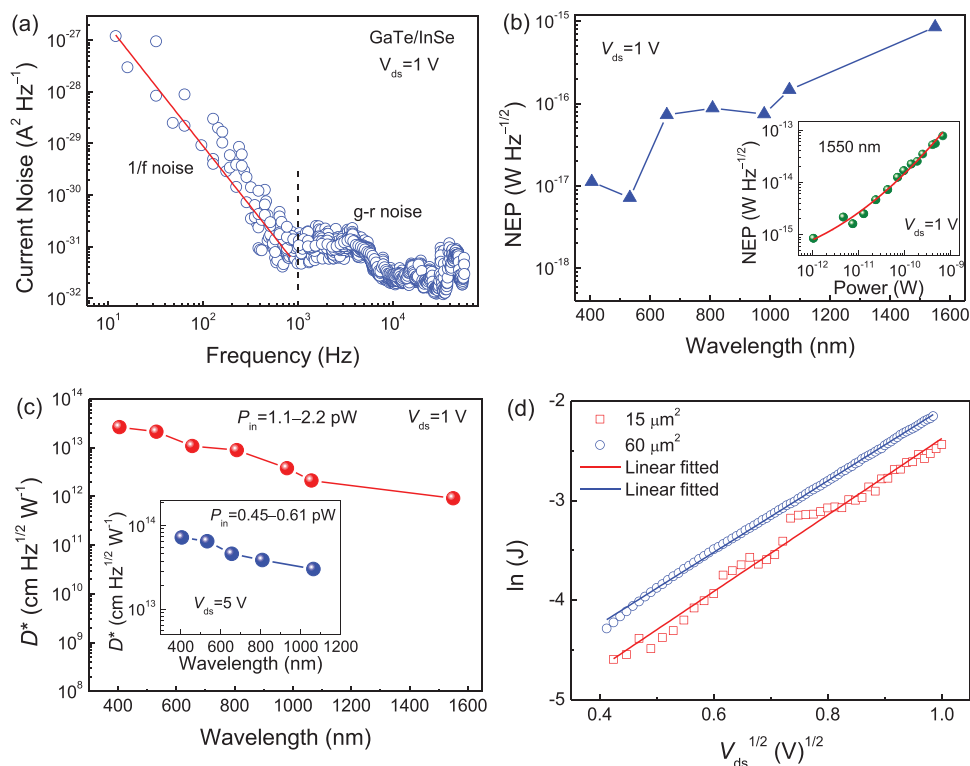


Figure 5. Noise and detectivity of the GaTe/InSe vdW heterostructure at SWIR. a) Spectra of current noise power density at $V_g = 0$ V and $V_{ds} = 1$ V. Linear fitting of the noise spectra in frequency less than 1 kHz (red line) indicates a $1/f$ noise of the devices in low frequency. b) NEP versus the excitation wavelength obtained at $V_{ds} = 1$ V. Inset: NEP as a function of illumination power under 1550 nm laser at $V_{ds} = 1$ V. c) D^* as a function of the wavelength obtained at $V_{ds} = 1$ V and $V_{ds} = 5$ V (inset). d) The curve of $\ln(J)$ versus the square root of the bias voltage $V_{ds}^{1/2}$. A linear fit indicates that the mechanism of the dark current is dominated by thermionic emission.

5–10 mA cm^{−2} at room temperature).^[7] The heteroepitaxial growth of the conventional complex type-II superlattices and quantum wells may result in strained (or defective) interfaces and dangling bonds (interfacial traps) which can result in the large dark current (the dark current is dominated substantially by the tunneling current) at room temperature, which limits the improvement of the D^* .^[7] This is also why they work at cryogenic temperatures to ensure high performance. In contrast, 2D material vdW heterostructures produced by layer-by-layer vertical dry stacking can ensure the lattice integrity (no dangling bonds) and interface cleanliness (almost no interfacial traps) of each layer. Further, we analyzed the dark current mechanism of our device and found that the dark current is dominated by thermionic emission according to the following equation^[50]

$$J = A^* T^2 \exp\left(-\frac{q\phi_b}{kT}\right) \exp\left(\frac{qV}{kT}\right) \quad (2)$$

where A^* is the effective Richardson constant, $A^* = 4 q m^* k^2 / h^3$, m^* is the effective electron mass, ϕ_b is the Schottky barrier height, k is the Boltzmann constant, and h is the Planck constant. Obviously, a linear fit for the relationship of $\ln(J) - V_{ds}^{1/2}$ indicates that the mechanism of the dark current is dominated by thermionic emission (Figure 5d), which indicates that the energy barrier at the 2D p–n vdW heterostructures can effectively suppress the dark current at room temperature compared to the tunneling mechanism in the

conventional complex type-II superlattices and quantum wells devices.^[7,51] This also depresses the random transport of the photogenerated carriers and therefore inhibits the undesired $1/f$ noise and generation–recombination noise. In addition, the GaTe/InSe vdW heterostructure photodetectors have an excellent R_i value at SWIR under an ultralow incident illumination (Figure 4b,c), which is comparable to that reported on the traditional semiconductors, such as the HgCdTe,^[6] InAs/GaSb type-II superlattices,^[6] InGaAs/GaAsSb type-II quantum wells,^[52] waveguide integrated Ge p–i–n photodetectors,^[53] InGaAs diode,^[1,54] and the emerging graphene-based SWIR photodetectors (Table S1, Supporting Information). Therefore, a low noise together with the excellent photoresponse enables this 2D GaTe/InSe vdW heterojunction device to achieve an ultrahigh specific detectivity D^* .

3. Conclusion

In summary, we have fabricated the GaTe/InSe vdW heterostructures using a layer-by-layer dry transfer method. Excitingly, these devices exhibit extraordinary detectivity in SWIR (1.0–1.55 μm) photodetection, which is beyond the cutoffs of the intrinsic bandgaps of the individual GaTe and InSe. This is enabled by the formation of the interlayer transition in the type-II band alignment. This argument is supported by the DFT calculation of the electronic structure of the GaTe/InSe vdW

heterostructures, which shows the effect of the InSe addition onto GaTe layers in lowering its bandgap. The GaTe/InSe photodetector exhibits extraordinary performances at room temperature including high responsivity up to 267.4 A W^{-1} at 1064 nm and 1.5 A W^{-1} at 1550 nm, and high detectivity D^* up to 10^{14} Jones at 1064 nm and 10^{12} Jones at 1550 nm. The unprecedented D^* under SWIR illumination is not only comparable to that of the state-of-the-arts commercial SWIR photodetectors based on InGaAs and InAs narrow-bandgap semiconductors, HgCdTe, InAs/GaSb type-II superlattices and InGaAs/GaAsSb type-II quantum wells (10^{11} – 10^{12} Jones at 1550 nm), but also 2–3 orders of magnitude higher than the best-reported result in 2D vdW heterostructure photodetectors. These results illustrate the promise of devising 2DLM vdW heterostructures with the interlayer transition for uncooled SWIR or even mid/far-infrared photodetectors.

4. Experimental Section

Fabrication of the GaTe/InSe vdW Heterostructure SWIR Photodetectors: Bulk GaTe single crystals were grown by the conventional high-temperature solution method with Ga as the flux. The Ga (purity 99.99%) and Te (purity 99.99%) blocks were placed in a clean alumina crucible with the ration of Ga:Te = 92:8. Then the alumina crucible was sealed in a quartz tube in an Ar environment. The quartz tube was first heated up in the furnace to 780 °C, held for 5 h and cooled down to 150 °C at a rate of 5 °C h^{-1} at last. After this heating procedure, the quartz tube was taken out quickly and then was decanted into the centrifuge to remove the excess Ga flux from GaTe single crystals. Bulk InSe single crystals were prepared by the Bridgman method, referring to the method described by Sucharitul et al.^[55,56]

Before layer-by-layer dry transfer, 5/30 nm Cr/Au was preferentially deposited onto the precleaned surface of SiO₂ (285 nm)/Si substrates as the source and drain electrodes by using an electron-beam lithography process (FEI-NOVA NanoSEM50 with JC Nabity-Nanometer Pattern Generation System) combined with thermal evaporation (DE400EVP, DE Technology). The devices were fabricated by mechanical exfoliation and targeted transfer method. First, the InSe and the GaTe flakes were prepared by a standard mechanical exfoliation method from the grown single crystals in the glove box. Then, the InSe and GaTe flakes were transferred layer by layer onto the SiO₂/Si substrate with Cr/Au electrodes using adhesive tapes and polydimethylsiloxane (PDMS) as a medium. In detail, the InSe flake was first prepared by mechanical exfoliation methods from the single crystals to the PDMS and then was transferred directionally onto the target substrate, in which the InSe flake covered a portion of the electrode. The GaTe flake was subsequently transferred to the surface of the InSe to form an overlap region of the GaTe and InSe, i.e., GaTe/InSe vdW p–n junctions. The layer numbers and quality of the samples were characterized by using Raman spectroscopy with 532 nm laser (LabRAM HR Evolution) combining with the AFM (AFM 5500, Keysight).

DFT Calculation on the Hybrid Structure of GaTe/InSe: The electronic structure of the monolayer and bulk InSe and GaTe as well as hybrid structures were calculated at the DFT level using either the Bloechl's tetrahedron and/or Gaussian smearing (GS) method. The details of the procedures for the DFT calculations on the 2D/nanostructures are given in the Supporting Information.

Characterization of Optoelectronic Performance: All measurements were taken at room temperature in the atmosphere. Current and voltage measurements were taken using a semiconductor parameter analyzer with four current amplifiers (4200-SCS, Keithley). The light sources were provided by using various continuous-wave semiconductor lasers with various excitation wavelengths range from 405 to 1550 nm. The incident light power was calibrated using an optical power meter

(1936-R, Newport) with two detectors, including a UV-enhanced silicon detector (918D-UV-OD3R, Newport) for 400–1064 nm and a germanium detector (918D-IR-OD3R, Newport) for 1550 nm. During the measurement, an optical collimating lens (k9) was connected to an optical fiber output in order to obtain a quasiparallel light beam, which was used to light illumination and the spot area (diameter of 10–15 mm) was larger than the device size for uniformity. The device was packaged in a sealed metal box (connecting the device electrodes through the bayonet-nut-connector), and the box was reopened a small hole (diameter of 1–2 mm) in order to allow the beam to pass through and illuminate the whole device surface without complication of room light. The incident light power (P_{in} with unit of W) illuminated on the actual devices was calculated by $P_{in} = P_d / A$, where P_d is the incident power density determined by dividing the quasiparallel light beam output power by the area of the beam and A is the actual photoactive area of the devices. Finally, the responsivity (R_i) can be obtained by $R_i = I_{ph}/P_{in} = I_{ph}/(P_d / A)$. The noise spectra of devices were characterized in the dark using a dynamic signal analyzer (SR785, Stanford Research) combined with a voltage source (2636B, Keithley). The dynamic photoresponse was measured using a digital oscilloscope (RTO1024, Rohde and Schwarz) together with an optical chopper (SR540, Stanford Research)

Supporting Information

Supporting Information is available from the Wiley Online Library or from the author.

Acknowledgements

T.L.Q. and Y.P.G. contributed equally to this work. The work was supported by the Shenzhen Science and Technology Innovation Commission (Grant Nos. JCYJ20170817110751776 and JCYJ20170307105434022) and the Guangdong Innovative and Entrepreneurial Research Team Program (Grant No. 2016ZT06D348). R.C. acknowledges the supports from the National Natural Science Foundation of China (Grant No. 11574130) and the Shenzhen Science and Technology Innovation Commission (Grant Nos. KQJSCX20170726145748464 and JCYJ20180305180553701). J.Z.W. acknowledges support by the US National Science Foundation (Contracts Nos. NSF-DMR-1909292, NSF-ECCS-1809293, and NSF-DMR-1508494) and the United States Army Research Office (Contract No. ARO-W911NF-16-1-0029).

Conflict of Interest

The authors declare no conflict of interest.

Keywords

2D materials, broadband photodetectors, interlayer transitions, shortwave infrared, vdW heterostructures

Received: July 15, 2019
Revised: September 8, 2019
Published online: October 21, 2019

- [1] A. Rogalski, *Prog. Quantum Electron.* **2003**, 27, 59.
- [2] J.-M. Liu, *Photonic Devices*, Cambridge University Press, New York, NY **2005**.
- [3] Y. P. Gong, P. Adhikari, Q. F. Liu, T. Wang, M. G. Gong, W. L. Chan, W. Y. Ching, J. D. Wu, *ACS Appl. Mater. Interfaces* **2017**, 9, 11016.

- [4] Y. P. Gong, Q. F. Liu, M. G. Gong, T. Wang, G. G. Zeng, W. L. Chan, J. D. Wu, *Adv. Opt. Mater.* **2017**, *5*, 1600478.
- [5] M. G. Gong, Q. F. Liu, R. Goul, D. Ewing, M. Casper, A. Stramel, A. Elliot, J. Z. Wu, *ACS Appl. Mater. Interfaces* **2017**, *9*, 27801.
- [6] C. Downs, T. E. Vandervelde, *Sensors* **2013**, *13*, 5054.
- [7] S. D. Gunapala, D. R. Rhiger, C. Jagadish, *Advances in Infrared Photodetectors*, Vol. 84, Academic Press, San Diego, CA **2011**.
- [8] K. Kang, K. H. Lee, Y. M. Han, H. Gao, S. E. Xie, D. A. Muller, J. Park, *Nature* **2017**, *550*, 229.
- [9] M. Massicotte, P. Schmidt, F. Violla, K. G. Schadler, A. Reserbat-Plantey, K. Watanabe, T. Taniguchi, K. J. Tielrooij, F. H. L. Koppens, *Nat. Nanotechnol.* **2016**, *11*, 42.
- [10] F. N. Xia, H. Wang, D. Xiao, M. Dubey, A. Ramasubramaniam, *Nat. Photonics* **2014**, *8*, 899.
- [11] L. Britnell, R. V. Gorbachev, R. Jalil, B. D. Belle, F. Schedin, A. Mishchenko, T. Georgiou, M. I. Katsnelson, L. Eaves, S. V. Morozov, N. M. R. Peres, J. Leist, A. K. Geim, K. S. Novoselov, L. A. Ponomarenko, *Science* **2012**, *335*, 947.
- [12] P. Rivera, K. L. Seyler, H. Y. Yu, J. R. Schaibley, J. Q. Yan, D. G. Mandrus, W. Yao, X. D. Xu, *Science* **2016**, *351*, 688.
- [13] S. X. Yang, C. Wang, C. Ataca, Y. Li, H. Chen, H. Cai, A. Suslu, J. C. Grossman, C. B. Jiang, Q. Liu, S. Tongay, *ACS Appl. Mater. Interfaces* **2016**, *8*, 2533.
- [14] K. A. Zhang, T. N. Zhang, G. H. Cheng, T. X. Li, S. X. Wang, W. Wei, X. H. Zhou, W. W. Yu, Y. Sun, P. Wang, D. Zhang, C. G. Zeng, X. J. Wang, W. D. Hu, H. J. Fan, G. Z. Shen, X. Chen, X. F. Duan, K. Chang, N. Dai, *ACS Nano* **2016**, *10*, 3852.
- [15] D. H. Luong, H. S. Lee, G. P. Neupane, S. Roy, G. Ghimire, J. H. Lee, Q. A. Vu, Y. H. Lee, *Adv. Mater.* **2017**, *29*, 1701512.
- [16] P. Rivera, J. R. Schaibley, A. M. Jones, J. S. Ross, S. F. Wu, G. Aivazian, P. Klement, K. Seyler, G. Clark, N. J. Ghimire, J. Q. Yan, D. G. Mandrus, W. Yao, X. D. Xu, *Nat. Commun.* **2015**, *6*, 6242.
- [17] A. T. Hanbicki, H. J. Chuang, M. R. Rosenberger, C. S. Hellberg, S. V. Sivaram, K. M. McCreary, I. I. Mazin, B. T. Jonker, *ACS Nano* **2018**, *12*, 4719.
- [18] M. Okada, A. Kutana, Y. Kureishi, Y. Kobayash, Y. Saito, T. Saito, K. Watanabe, T. Taniguchi, S. Gupta, Y. Miyata, B. I. Yakobson, H. Shinohara, R. Kitaura, *ACS Nano* **2018**, *12*, 2498.
- [19] T. Deilmann, K. S. Thygesen, *Nano Lett.* **2018**, *18*, 2984.
- [20] T. Deilmann, K. S. Thygesen, *Nano Lett.* **2018**, *18*, 1460.
- [21] M. Baranowski, A. Surrente, L. Klopotoski, J. M. Urban, N. Zhang, D. K. Maude, K. Wiwatowski, S. Mackowski, Y. C. Kung, D. Dumcenco, A. Kis, P. Plochocka, *Nano Lett.* **2017**, *17*, 6360.
- [22] H. L. Chen, X. W. Wen, J. Zhang, T. M. Wu, Y. J. Gong, X. Zhang, J. T. Yuan, C. Y. Yi, J. Lou, P. M. Ajayan, W. Zhuang, G. Y. Zhang, J. R. Zheng, *Nat. Commun.* **2016**, *7*, 12512.
- [23] Y. G. Wang, X. W. Huang, D. Wu, R. R. Zhuo, E. P. Wu, C. Jia, Z. F. Shi, T. T. Xu, Y. T. Tian, X. J. Li, *J. Mater. Chem. C* **2018**, *6*, 4861.
- [24] S. H. Jo, H. W. Lee, J. Shim, K. Heo, M. Kim, Y. J. Song, J. H. Park, *Adv. Sci.* **2018**, *5*, 1700423.
- [25] D. A. Bandurin, A. V. Tyurnina, G. L. Yu, A. Mishchenko, V. Zolyomi, S. V. Morozov, R. K. Kumar, R. V. Gorbachev, Z. R. Kudrynskiy, S. Pezzini, Z. D. Kovalyuk, U. Zeitler, K. S. Novoselov, A. Patané, L. Eaves, I. V. Grigorieva, V. I. Fal'ko, A. K. Geim, Y. Cao, *Nat. Nanotechnol.* **2017**, *12*, 223.
- [26] C. Y. Song, F. R. Fan, N. N. Xuan, S. Y. Huang, G. W. Zhang, C. Wang, Z. Z. Sun, H. Wu, H. G. Yan, *ACS Appl. Mater. Interfaces* **2018**, *10*, 3994.
- [27] F. Wang, Z. X. Wang, K. Xu, F. M. Wang, Q. S. Wang, Y. Huang, L. Yin, J. He, *Nano Lett.* **2015**, *15*, 7558.
- [28] Y. H. Sun, S. L. Luo, X. G. Zhao, K. Biswas, S. L. Li, L. J. Zhang, *Nanoscale* **2018**, *10*, 7991.
- [29] W. Feng, Z. Jin, J. Yuan, J. Zhang, S. Jia, L. Dong, J. Yoon, L. Zhou, R. Vajtai, J. M. Tour, P. M. Ajayan, P. Hu, J. Lou, *2D Mater.* **2018**, *5*, 025008.
- [30] P. Matheswaran, R. Sathyamoorthy, K. Asokan, *Electron. Mater. Lett.* **2012**, *8*, 621.
- [31] V. N. Katerinchuk, M. Z. Kovalyuk, *Tech. Phys. Lett.* **1999**, *25*, 54.
- [32] G. Kresse, J. Hafner, *Phys. Rev. B* **1993**, *47*, 558.
- [33] G. Kresse, J. Furthmuller, *Comput. Mater. Sci.* **1996**, *6*, 15.
- [34] G. Kresse, J. Furthmuller, *Phys. Rev. B* **1996**, *54*, 11169.
- [35] G. Kresse, J. Hafner, *Phys. Rev. B* **1994**, *49*, 14251.
- [36] M. Dion, H. Rydberg, E. Schroder, D. C. Langreth, B. I. Lundqvist, *Phys. Rev. Lett.* **2004**, *92*, 246401.
- [37] M. G. Gong, R. Sakidja, Q. F. Liu, R. Goul, D. Ewing, M. Casper, A. Stramel, A. Elliot, J. Z. Wu, *Adv. Opt. Mater.* **2018**, *6*, 1701241.
- [38] J. P. Perdew, *Int. J. Quantum Chem.* **1985**, *28*, 497.
- [39] A. V. Krukau, O. A. Vydrov, A. F. Izmaylov, G. E. Scuseria, *J. Chem. Phys.* **2006**, *125*, 224106.
- [40] A. Castellanos-Gomez, *J. Phys. Chem. Lett.* **2015**, *6*, 4280.
- [41] S. X. Huang, Y. Tatsumi, X. Ling, H. H. Guo, Z. Q. Wang, G. Watson, A. A. Puzos, D. B. Geohegan, J. Kong, J. Li, T. Yang, R. Saito, M. S. Dresselhaus, *ACS Nano* **2016**, *10*, 8964.
- [42] S. D. Lei, L. H. Ge, S. Najmaei, A. George, R. Koppera, J. Lou, M. Chhowalla, H. Yamaguchi, G. Gupta, R. Vajtai, A. D. Mohite, P. M. Ajayan, *ACS Nano* **2014**, *8*, 1263.
- [43] C. H. Lee, G. H. Lee, A. M. van der Zande, W. C. Chen, Y. L. Li, M. Y. Han, X. Cui, G. Arefe, C. Nuckolls, T. F. Heinz, J. Guo, J. Hone, P. Kim, *Nat. Nanotechnol.* **2014**, *9*, 676.
- [44] J. S. Ross, P. Rivera, J. Schaibley, E. Lee-Wong, H. Y. Yu, T. Taniguchi, K. Watanabe, J. Q. Yan, D. Mandrus, D. Cobden, W. Yao, X. D. Xu, *Nano Lett.* **2017**, *17*, 638.
- [45] H. Y. Yu, Y. Wang, Q. J. Tong, X. D. Xu, W. Yao, *Phys. Rev. Lett.* **2015**, *115*, 187002.
- [46] C. Xie, C. Mak, X. M. Tao, F. Yan, *Adv. Funct. Mater.* **2017**, *27*, 1603886.
- [47] M. S. Long, A. Y. Gao, P. Wang, H. Xia, C. Ott, C. Pan, Y. J. Fu, E. F. Liu, X. S. Chen, W. Lu, T. Nilges, J. B. Xu, X. M. Wang, W. D. Hu, F. Miao, *Sci. Adv.* **2017**, *3*, e1700589.
- [48] L. Ye, H. Li, Z. F. Chen, J. B. Xu, *ACS Photonics* **2016**, *3*, 692.
- [49] M. S. Long, E. F. Liu, P. Wang, A. Y. Gao, H. Xia, W. Luo, B. G. Wang, J. W. Zeng, Y. J. Fu, K. Xu, W. Zhou, Y. Y. Lv, S. H. Yao, M. H. Lu, Y. F. Chen, Z. H. Ni, Y. M. You, X. A. Zhang, S. Q. Qin, Y. Shi, W. D. Hu, D. Y. Xing, F. Miao, *Nano Lett.* **2016**, *16*, 2254.
- [50] S. M. Sze, K. K. Ng, *Physics of Semiconductor Devices 3rd Edition*, John Wiley & Sons, Hoboken, NJ **2006**.
- [51] K. Y. Cheong, J. H. Moon, H. J. Kim, W. Bahng, N. K. Kim, *J. Appl. Phys.* **2008**, *103*, 084113.
- [52] B. Tossoun, R. Stephens, Y. Wang, S. Addamane, G. Balakrishnan, A. Holmes, A. Beling, *IEEE Photonics Technol. Lett.* **2018**, *30*, 399.
- [53] J. Michel, J. F. Liu, L. C. Kimerling, *Nat. Photonics* **2010**, *4*, 527.
- [54] A. Rogalski, R. Ciupa, *J. Electron. Mater.* **1999**, *28*, 630.
- [55] S. Sucharitakul, N. J. Goble, U. R. Kumar, R. Sankar, Z. A. Bogorad, F. C. Chou, Y. T. Chen, X. P. A. Gao, *Nano Lett.* **2015**, *15*, 3815.
- [56] T. Ishii, *J. Cryst. Growth* **1988**, *89*, 459.